PHYSICAL REVIEW D **93,** 054507 (2016)

Roberge-Weiss transition in $N_f = 2$ QCD with Wilson fermions and $N_\tau = 6$

Christopher Czaban,[1,2,*] Francesca Cuteri,[1,†] Owe Philipsen,[1,2,‡] Christopher Pinke,[1,§] and Alessandro Sciarra[1,‖]

[1]*Institut für Theoretische Physik—Johann Wolfgang Goethe-Universität, Germany Max-von-Laue-Str. 1, 60438 Frankfurt am Main*

[2]*John von Neumann Institute for Computing (NIC) Gesellschaft für Schwerionenforschung (GSI), Planckstr. 1, 64291 Darmstadt, Germany*

(Received 7 January 2016; published 21 March 2016)

QCD with imaginary chemical potential is free of the sign problem and exhibits a rich phase structure constraining the phase diagram at real chemical potential. We simulate the critical end point of the Roberge-Weiss transition at imaginary chemical potential for $N_f = 2$ QCD on $N_\tau = 6$ lattices with standard Wilson fermions. As found on coarser lattices, the Roberge-Weiss end point is a triple point connecting the deconfinement/chiral transitions in the heavy/light quark mass region and changes to a second-order end point for intermediate masses. These regimes are separated by two tricritical values of the quark mass, which we determine by extracting the critical exponent ν from a systematic finite size scaling analysis of the Binder cumulant of the imaginary part of the Polyakov loop. We are able to explain a previously observed finite size effect afflicting the scaling of the Binder cumulant in the regime of three-phase coexistence. Compared to $N_\tau = 4$ lattices, the tricritical masses are significantly shifted. Exploratory results on $N_\tau = 8$ as well as comparison with staggered simulations suggest that much finer lattices are needed before a continuum extrapolation becomes feasible.

DOI: 10.1103/PhysRevD.93.054507

I. INTRODUCTION

One of the most challenging aspects of modern particle physics is to map out the phase diagram of QCD as a function of temperature T and baryon chemical potential μ_B. Due to the nonperturbative nature of the strong interactions on hadronic energy scales, a first principles approach such as Lattice QCD is mandatory.

At zero baryon chemical potential, standard Monte Carlo simulations can be applied. In order to understand the interplay between confinement and chiral symmetry breaking and their influence on the thermal transition, it is interesting to study the QCD phase diagram varying the quark masses between the chiral ($m \to 0$) and quenched ($m \to \infty$) limits. For $N_f = 2$, 3 degenerate quark flavors, regions of first-order chiral and deconfinement transitions are seen on coarse $N_\tau = 4$, 6 lattices with standard actions for light and heavy quark masses, respectively, whereas intermediate mass regions including the physical point show crossover behavior. For improved actions, the chiral first-order region is significantly smaller, but presently no continuum extrapolation of any of these features is available (see Ref. [1] and references therein for a recent overview).

At finite μ_B, the sign problem prevents importance sampling techniques, and alternative strategies must be used. One possibility is to introduce a purely imaginary quark chemical potential $\mu \equiv \mu_B/3 = \imath\mu_i$ ($\mu_i \in \mathbb{R}$), for which no sign problem is present. The phase structure at imaginary chemical potential constrains the situation at real μ_B by analytic continuation.

In the last decade, a first understanding of the QCD phase diagram at imaginary chemical potential has been developed as summarized in Sec. II. It is so far based on investigations on coarse lattices ($N_\tau = 4$, $a \sim 0.3$ fm) with staggered fermions [2–4] and standard [5] or improved [6] Wilson fermions only. In the present work, we repeat the study made in Ref. [5] on a finer lattice ($N_\tau = 6$, $a \sim 0.2$ fm). Unfortunately, we find that several further and more costly simulations are required before any continuum extrapolation can be attempted.

After a brief description of the QCD phase diagram in Sec. II, we illustrate our simulation setup in Sec. III. Section IV is dedicated to a study of the qualitative behavior of the Binder cumulant, which explains some puzzling finite size effects observed in earlier studies. The results of our investigation are presented and discussed in Sec. V.

II. QCD PHASE DIAGRAM AT IMAGINARY CHEMICAL POTENTIAL

The QCD phase diagram for purely imaginary values of the chemical potential $\mu = \imath\mu_i$ has a rich structure that depends on the temperature T, chemical potential μ_i as well as on the number of flavors and the values of the quark masses.

The QCD partition function is symmetric by reflection in μ, and it is periodic in μ_i/T with period $2\pi/N_c$ [7]. These

*czaban@th.physik.uni-frankfurt.de
†cuteri@th.physik.uni-frankfurt.de
‡philipsen@th.physik.uni-frankfurt.de
§pinke@th.physik.uni-frankfurt.de
‖sciarra@th.physik.uni-frankfurt.de

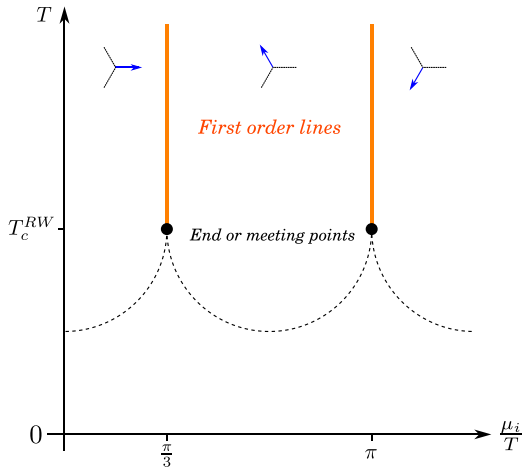

FIG. 1. QCD phase diagram in the $T-\mu_i$ plane. The dashed line depicts the chiral/deconfinement transition of which the nature depends on the quark masses. The orange lines represent the Roberge-Weiss transitions. The black dots, where the first-order lines terminate, can be first-order triple points, tricritical points or second-order end points.

two properties imply the phase structure depicted qualitatively in Fig. 1 (from now on, we fix $N_c = 3$). In particular, varying the imaginary chemical potential, phase transitions between different $Z(3)$ sectors are crossed at fixed values ${\mu_i}^c/T = (2k+1)\pi/3$ with $k \in \mathbb{Z}$ (the so-called Roberge-Weiss transitions). Such transitions are smooth crossovers for low T and true first-order phase transitions for high T [7]. Any physical observable is invariant under a change of the $Z(3)$ center sector (i.e. shifting μ_i/T by its period), which can be distinguished by the phase of the Polyakov loop L. For any spatial lattice site $\mathbf{n}$,

$$L(\mathbf{n}) = \frac{1}{3}\mathrm{Tr}_C\left[\prod_{n_0=0}^{N_\tau-1} U_0(n_0,\mathbf{n})\right] \equiv |L(\mathbf{n})|e^{-\imath\varphi}, \qquad (1)$$

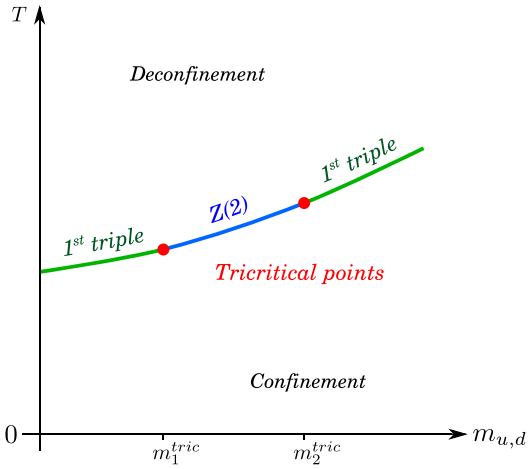

FIG. 2. QCD phase diagram in the $T-m_{u,d}$ plane for a fixed critical value of the imaginary critical potential $\mu_i = {\mu_i}^c$.

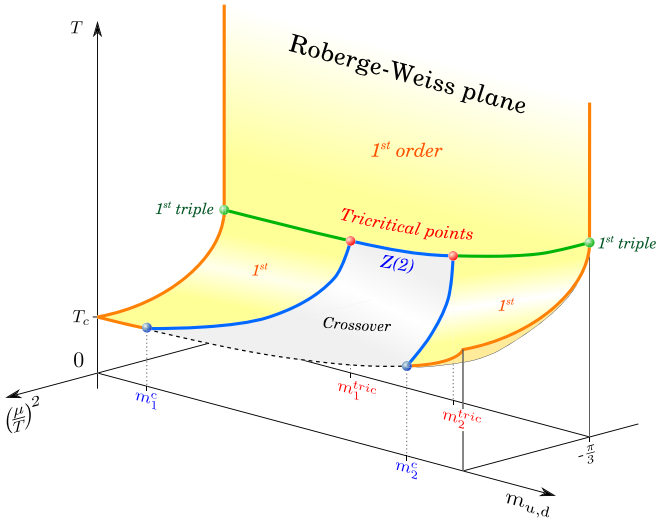

FIG. 3. $N_f = 2$ QCD phase diagram in the $T-\mu-m_{u,d}$ space for $-\frac{\pi}{3} \le (\frac{\mu}{T})^2 \le 0$.

where, as different sectors are explored, the phase φ takes the values $\langle\varphi\rangle = 2n\pi/3$ with $n \in \{0,1,2\}$. The dashed line in Fig. 1 represents the analytic continuation of the chiral/deconfinement transition which is crossed varying the temperature. Its type depends on the values of the quark masses. Consequently, also the nature of the meeting points of the dashed line and the first-order Roberge-Weiss lines is mass dependent. Recent studies [2–4] show that, for $N_f = 2$ and $N_f = 3$ on coarse lattices, these points are first-order triple points for small and large masses, while they are second-order end points for intermediate masses. Therefore, there are two tricritical points separating the two regimes. This has been schematically drawn in Fig. 2.

Figure 3 combines Figs. 1 and 2 into a 3D picture. On coarse lattices, the first-order chiral transition region extends through $\mu = 0$, producing a critical point m_1^c in the $T-m_{u,d}$ plane [8,9]. Slicing Fig. 3 at $m_{u,d} = \text{const}$ allows us to understand how the nature of the dashed line of Fig. 1 changes. Figure 3 has been drawn for $0 < \mu_i < \pi/3$; the situation at any other value of μ_i can be deduced using the symmetries of the partition function. Note that the position of the (tri)critical points and thus also the shape of the $Z(2)$ lines changes as the continuum limit is approached. Reducing the lattice spacing, the low mass first-order region shrinks [10], while the high mass one enlarges [11]. Similarly, the tricritical masses measured in physical units on $N_\tau = 4$ lattices have rather different values in different fermion discretizations [4,9]. The present work is a first step toward understanding the cutoff effects in the Wilson formulation.

III. SIMULATION SETUP

After performing the integration over the fermionic fields, the QCD grand-canonical partition function with

$N_f = 2$ mass-degenerate quarks in the presence of an imaginary chemical potential μ_i reads

$$\mathcal{Z}(T,\mu_i) = \int \mathcal{D}U e^{-\mathcal{S}_g[U]} (\det D[U,\mu_i])^2,$$

where $\mathcal{S}_g$ is the gauge part of the action and D is the fermion matrix. For our study, we used the standard Wilson gauge action,

$$\mathcal{S}_g[U] = \beta \sum_P \{1 - \Re[\mathrm{Tr}_C P]\},$$

and the standard Wilson discretization of dynamical fermions, with the fermion matrix

$$D_{i,j} = \delta_{i,j} - \kappa \sum_{\rho=\pm 0}^{\pm 3} e^{\imath a \mu_i \cdot \delta_{|\rho|,0} \cdot \mathrm{sgn}(\rho)} [(1-\gamma_\rho) U_\rho(i) \delta_{i+\hat{\rho},j}].$$

In the last two equations, β is the lattice coupling (related to the bare coupling g via $\beta = 6/g^2$), P indicates the plaquette, i and j refer to lattice sites, $\hat{\rho}$ is a unit vector on the lattice and a is the lattice spacing. Moreover, $\gamma_{-\rho} \equiv -\gamma_\rho$, and $U_{-\rho}(i) \equiv U_\rho^\dagger(i - \vec{\rho})$. The bare quark mass $m_{u,d} \equiv m$ is contained in the hopping parameter κ via

$$\kappa = \frac{1}{2(am+4)}.$$

The shifted phase $\phi = \varphi - \mu_i/T$ of the Polyakov loop is an order parameter to distinguish between the low T disordered phase and the high T ordered phase with two-state coexistence [2]. For the particular, critical values $\mu_i/T = \pi \pm 2\pi k$, $k \in \mathbb{Z}$, also the imaginary part of the Polyakov loop behaves as an order parameter. This is the reason why we fixed $\mu_i/T = \pi$ in all our simulations. Since the temperature on the lattice is given by

$$T = \frac{1}{a(\beta) N_\tau},$$

we have $a\mu_i = \pi/6$ for $N_\tau = 6$.

In order to identify the nature of the Roberge-Weiss end or meeting point, we use the Binder cumulant [12], defined as

$$B_4(X, \alpha_1, \ldots, \alpha_n) \equiv \frac{\langle (X - \langle X \rangle)^4 \rangle}{\langle (X - \langle X \rangle)^2 \rangle^2},$$

where X is a general observable and $\alpha_1, \ldots, \alpha_n$ is a set of parameters on which B_4 depends. Critical parameter values α_i^c are defined by the vanishing of the third moment of the fluctuations. In the thermodynamic limit $V \to \infty$, i.e. when nonanalytic phase transitions can exist, the Binder cumulant evaluated at critical couplings then takes different values depending on the nature of the phase transition (see Table I).

TABLE I. Critical values of ν, γ and $B_4 \equiv B_4(X, \alpha_c)$ for some universality classes [13].

	Crossover	1st triple	Tricritical	3D Ising
B_4	3	1.5	2	1.604
ν	⋯	1/3	1/2	0.6301(4)
γ	⋯	1	1	1.2372(5)

In our study, we choose $X = L_{\mathrm{Im}}$ [in the following, L stands for the spatially averaged $L(\mathbf{n})$ of Eq. (1)] and $\{\alpha_i\} = \{\beta, \kappa, \mu_i\}$. Since we work at the critical value $\mu_i = \pi T$, then, at any value of the temperature, $\langle (X - \langle X \rangle)^3 \rangle \approx 0$, and we expect the Binder cumulant to be close to 3 (crossover) for low T and close to 1 (first order) for high T. Even though B_4 is a nonanalytic step function for $V \to \infty$, at finite volume it gets smoothed out, and its slope increases with the volume. Around the critical coupling β_c, the Binder cumulant is expected to show a well-defined finite size scaling behavior. It is then a function of $x \equiv (\beta - \beta_c) N_\sigma^{1/\nu}$ only and can be Taylor expanded as

$$B_4(\beta, N_\sigma) = B_4(\beta_c, \infty) + a_1 x + a_2 x^2 + \mathcal{O}(x^3). \quad (2)$$

Close to the thermodynamic limit, the intersection of different volumes gives β_c, and the critical exponent ν takes its universal value depending on the type of transition. In Table I, the values of the critical exponents relevant for our work have been summarized [13].

Another important quantity is the order parameter susceptibility, defined as

$$\chi(X) \equiv N_\sigma^3 \langle (X - \langle X \rangle)^2 \rangle.$$

Also this quantity is expected to scale around β_c according to

$$\chi = N_\sigma^{\gamma/\nu} f(t N_\sigma^{1/\nu}), \quad (3)$$

where $t \equiv (T - T_c)/T_c$ is the reduced temperature and f a universal scaling function. This means that, once the critical exponents γ and ν are fixed to the correct values, $\chi/N_\sigma^{\gamma/\nu}$ measured on different lattice sizes should collapse when plotted against $tN_\sigma^{1/\nu}$. We also performed occasional cross-checks of the susceptibility for $X = \langle \overline{\psi}\psi \rangle$ leading to fully consistent results.

Our strategy to locate the two tricritical values of κ is completely analogous to that used in Ref. [5]. For each simulated value of κ, we measured the Binder cumulant in the critical region and extracted the values of $B_4(\beta_c, \infty)$, a_1, β_c and ν fitting our data according to Eq. (2), considering

the linear term only. The changes in ν as κ is varied allow us to locate the tricritical points.

We studied nine values of the bare quark mass between $\kappa = 0.1$ and $\kappa = 0.165$. For each value of κ, we simulated at the fixed temporal lattice extent $N_\tau = 6$ that implies the value $a\mu_i = \pi/6$ for the imaginary chemical potential. Three or four different spatial lattice sizes per κ have been used, always with $N_\sigma \geq 16$ (except for $\kappa = 0.1625$ where also $N_\sigma = 12$ was used). This gives a minimal aspect ratio of almost 3. For every lattice size, 6 up to 30 values of β around the critical value have been simulated. Between 40k–500k standard Hybrid Monte Carlo [14] trajectories of unit length per β have been collected after at least 5k trajectories of thermalization. The observables of interest (i.e. plaquette, L_{Re} and L_{Im}) were measured for every trajectory after the thermalization. In each run, the acceptance rate was tuned to ~75%. For $\kappa \geq 0.16$, i.e. for the smallest masses, the Hasenbusch trick [15] in the integration of the molecular dynamics equations has been used to reduce the integrator instability, which is triggered by isolated small modes of the fermion kernel [16]. Because of the particularly delicate fitting procedure required to extract the critical exponent ν from Eq. (2), we almost always produced four different Markov chains for each value of the coupling in order to better understand if the collected statistics was enough. Ferrenberg-Swendsen reweighting [17] was used to smoothly interpolate between β-points (see Appendix B for more information about the method used to extract ν and Appendix A for the simulations details).

For scale-setting purposes, $T = 0$ simulations at or close to certain critical parameters have been performed. $\mathcal{O}(400)$ independent configurations on $16^3 \times 32$ lattices have been produced. The scale itself is then set by the Wilson flow parameter w_0 using the publicly available code described in Ref. [18]. This method is very efficient and fast. In addition, the pion mass m_π was determined using these configurations. See Table II for more details.

All our numerical simulations have been performed using the *publicly available* [19] OpenCL [20] based code CL^{2}QCD [21,22], which is optimized to run efficiently on GPUs. In particular, the LOEWE-CSC [23] at Goethe-University Frankfurt and the L-CSC [24] at Gesellschaft für Schwerionenforschung (GSI) in Darmstadt have been used.

IV. THE BINDER CUMULANT BUMP

As explained in Sec. III, the Binder cumulant is expected to change from 3 at low T to 1 at high T. It is also known that $B_4(\beta) = 2\Theta(\beta_c - \beta) + 1$ in the thermodynamic limit, where Θ is the Heaviside step function. On finite volumes, the discontinuity is smoothed out, and the Binder cumulant could naively be expected to be a monotonic function of β. However, it turns out that B_4 takes values higher than 3 at $\beta \lesssim \beta_c$ for small and large values of κ, i.e. in the first-order regions. In Fig. 4(a), the data for $\kappa = 0.165$ are shown, with a "bump" rising to values significantly larger than 3 on the crossover side of the transition. Note how the bump gets higher and narrower on larger volumes. Moreover, the β-region where B_4 changes from 3 to 1 shrinks as N_σ is increased, as expected for a first-order transition. The occurrence of the bump has been reported also in other studies [6]. This distorts the finite size analysis compared to the naive expectations and in particular leads to significantly higher values of the Binder cumulant at the intersection than expected in the thermodynamic limit [2,5,6]. Thus, the effect needs to be understood if one aims at results in the thermodynamic limit.

The described behavior can be explained by modelling the distributions at work in a situation with three phases. Let us consider the distribution of the imaginary part of the Polyakov loop on a finite volume for sufficiently high statistics: it is a normal distribution for $\beta \ll \beta_c$ (crossover), and it is the sum of two normal distributions with mean values $\pm|L_{\mathrm{Im}}|$ for $\beta \gg \beta_c$ (first order). This is clearly

TABLE II. Results of the scale setting ($T = 0$ simulations performed on $\mathrm{N}_\tau = 32$, $\mathrm{N}_\sigma = 16$ lattices). The number of independent configurations used is reported in the third column (`# confs`). w_0/a has been determined and converted to physical scales using the publicly available code described in Ref. [18]. For the pion mass determination, eight point sources per configuration have been used. The table also contains the lattice spacing, the pion mass and the temperature of the corresponding finite temperature ensemble in physical units.

κ	β	# confs	w_0/a	am_π	a [fm]	m_π [MeV]	N_τ	T [MeV]
0.0910	5.6655	1600	0.9161(6)	3.0107(2)	0.192(2)	3101(32)	4	258(3)
0.1000	5.6539	1600	0.9017(12)	2.7285(2)	0.195(2)	2766(29)		253(3)
0.1100	5.6341	1600	0.8789(10)	2.4250(3)	0.200(2)	2396(25)		247(3)
0.1575	5.3550	400	0.7104(3)	1.1426(17)	0.247(3)	913(9)		200(2)
0.1000	5.8698	1600	1.4650(20)	2.5793(6)	0.120(1)	4248(44)	6	275(3)
0.1100	5.8567	1600	1.4594(18)	2.2302(2)	0.120(1)	3659(38)		273(3)
0.1200	5.8287	1200	1.4333(20)	1.8862(4)	0.122(1)	3040(31)		269(3)
0.1600	5.4367	200	1.1248(14)	0.6045(15)	0.156(2)	764(8)		211(2)
0.1625	5.3862	200	1.0700(17)	0.5559(23)	0.164(2)	669(8)		201(2)
0.1650	5.3347	200	1.0082(13)	0.5184(27)	0.174(2)	588(7)		189(2)
0.1300	5.9590	1600	1.9357(44)	1.3896(2)	0.091(1)	3024(32)	8	272(3)

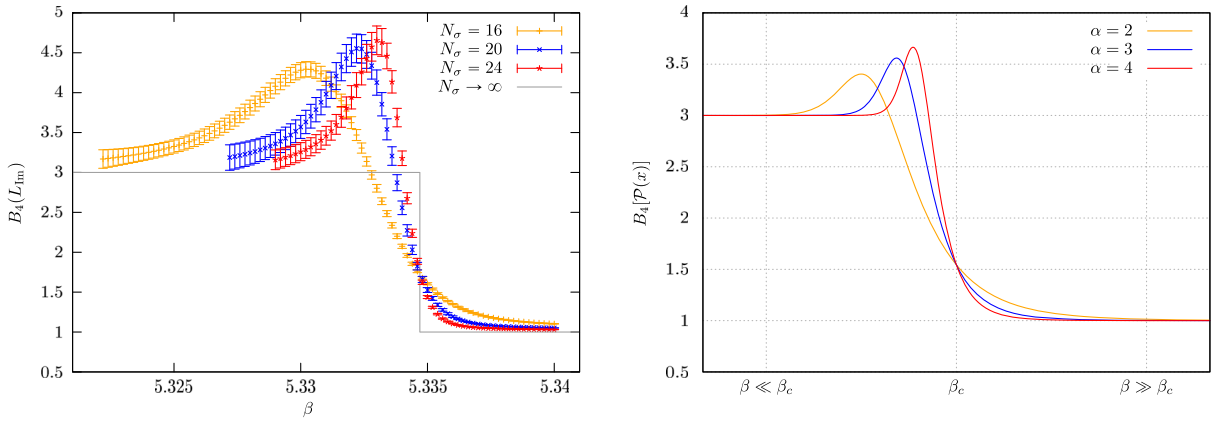

(a) Binder cumulant reweighted data for $\kappa = 0.165$. (b) Binder cumulant as function of β in our model.

FIG. 4. Comparison between the measured Binder cumulant of the imaginary part of the Polyakov loop and its analytic form in our model. Three different lattice spatial extents and three different values of the parameter α have been used. The gray line in the left plot is the expected behavior of $B_4(\beta)$ in the thermodynamic limit.

visible in Fig. 5(a), where histograms of $L_{\rm Im}$ are depicted. Around the transition, the $L_{\rm Im}$ distribution can be thought of as the sum of three Gaussian distributions, the weights of which depend on the temperature. We thus consider

$$\mathcal{P}(x) \equiv w_o \mathcal{N}(-d,\sigma) + w_i \mathcal{N}(0,\sigma) + w_o \mathcal{N}(d,\sigma), \quad (4)$$

where

$$\mathcal{N}(\mu,\sigma) \equiv \frac{1}{\sigma\sqrt{2\pi}} e^{-\frac{(x-\mu)^2}{2\sigma^2}}$$

is a Gaussian distribution with mean μ and variance σ^2, d is a positive real number, while w_o and w_i are the weights of the outer and inner distributions, respectively. Of course, $2w_o + w_i = 1$. Here, for simplicity, we assumed the three distributions to have the same variance. The symmetry of the outer distributions with respect to zero and the fact that their weight is the same are, instead, implied by the symmetries of the physical system. It is clear that d has to be a function of β as well as w_o and w_i. In particular, we have $w_o \approx 0$ and $d \approx 0$ for $\beta \ll \beta_c$, while $w_i \approx 0$ and $d \gg \sigma$, i.e. the outer Gaussian distributions are well separated, for $\beta \gg \beta_c$. With an analytic expression for the distribution, the value of the Binder cumulant for an even function can be explicitly calculated through

$$B_4[\mathcal{P}(x)] = \frac{\int_{-\infty}^{+\infty} x^4 \mathcal{P}(x) dx}{\left[\int_{-\infty}^{+\infty} x^2 \mathcal{P}(x) dx\right]^2},$$

and we will have indeed

$$B_4[\mathcal{P}_{\beta \ll \beta_c}(x)] = 3 \quad (5a)$$

while

$$B_4[\mathcal{P}_{\beta \gg \beta_c}(x)] = 3 - \frac{2d^4}{(d^2+\sigma^2)^2} \approx 1. \quad (5b)$$

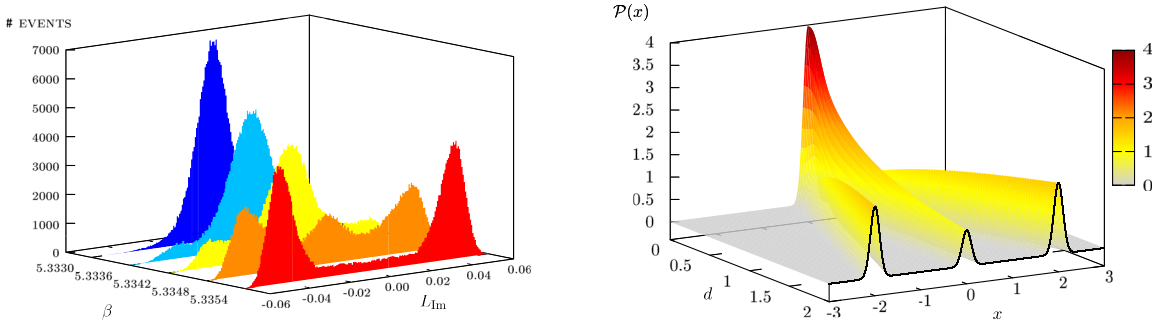

(a) Symmetrized histograms of $L_{\rm Im}$ for $\kappa = 0.165$ and $N_\sigma = 24$ at various values of β around β_c. (b) Modelled probability distribution of Eq. (4), plotted as function of d and x for fixed $\sigma = 0.1$ and $\alpha = 1$.

FIG. 5. Comparison between histograms of the imaginary part of the Polyakov loop and the corresponding probability distribution in the model. Note how d is related to β. For low (high) temperatures, only one (two) Gaussian distribution(s) is (are) present. Moreover, in (a), at $\beta = 5.3348$ (i.e. slightly after the transition), a clear three-peak structure is visible, as expected for a triple point. All these features are captured in the model.

Before trying to further connect our parameters d, w_o and w_i to β, let us just study how the Binder cumulant of our distribution changes as they are varied. At the end of the section, we will comment further on how the quantities in our simple model are related to the physical ones.

It is possible to think of the two cases in Eqs. (5) as the two limits $d \to 0$ and $d \to \infty$, on the condition that the weights of the distributions change accordingly. One way to realize this is to assume that both w_o and w_i are functions of d, satisfying the following conditions:

$$\lim_{d\to 0} w_i(d) = 1 \quad \text{and} \quad \lim_{d\to 0} w_o(d) = 0;$$
$$\lim_{d\to \infty} w_i(d) = 0 \quad \text{and} \quad \lim_{d\to \infty} w_o(d) = \frac{1}{2}.$$

Now, in order to properly model the weights to reproduce the bump of Fig. 4(a), we first have to understand how a Binder cumulant larger than 3 can arise. Leaving the weights of the three normal distributions completely general, it can be shown that

$$B_4[\mathcal{P}(x)] = 3 + \frac{2w_o d^4(w_i - 4w_o)}{(2w_o d^2 + \sigma^2)^2}.$$

Hence, when the weight of the central distribution is more than four times larger than the weight of the outer distributions, the Binder cumulant takes values larger than 3. It is then sufficient to choose the functions $w_o(d)$ and $w_i(d)$ to respect the limits above and in a way such that

$$w_i(d) > 4w_o(d) \tag{6}$$

for some values of d. A simple choice to respect the required asymptotic behavior is

$$w_i(d) = \frac{\frac{1}{\alpha d+1}}{\frac{1}{\alpha d+1} + 2(1 - \frac{1}{\frac{d}{\alpha}+1})} = \frac{\alpha + d}{\alpha + 3d + 2\alpha d^2}, \tag{7a}$$

$$w_o(d) = \frac{1 - \frac{1}{\frac{d}{\alpha}+1}}{\frac{1}{\alpha d+1} + 2(1 - \frac{1}{\frac{d}{\alpha}+1})} = \frac{d(1+\alpha d)}{\alpha + 3d + 2\alpha d^2}, \tag{7b}$$

where $\alpha > 0$ is a parameter to calibrate how fast the weights $w_i(d)$ and $w_o(d)$ change from 1 to 0 and from 0 to 1/2, respectively. More precisely, the larger the α, the quicker the inner (outer) Gaussian distribution(s) disappears (appear). In Fig. 5(b), it is shown how the distribution $\mathcal{P}(x)$ changes increasing the parameter d for $\sigma = 0.1$ and $\alpha = 1$. One clearly sees that for small d there is almost only the inner Gaussian. For higher d, the middle normal distribution gradually disappears. Thus d plays the role of temperature or β, and α that of the volume.

The region where the Binder cumulant is larger than 3 can be found by inserting Eqs. (7) in Eq. (6). Then, it follows that

$$B_4 > 3 \Leftrightarrow 0 < d < \frac{-3 + \sqrt{9 + 16\alpha^2}}{8\alpha}; \tag{8}$$

actually, using the chosen weights in Eq. (4), we get

$$B_4[\mathcal{P}(x)] = 3 - \frac{2d^5(1+\alpha d)(4\alpha d^2 + 3d - \alpha)}{[2d^3(1+\alpha d) + \sigma^2(\alpha + 3d + 2\alpha d^2)]^2},$$

which confirms what is expected in Eq. (8). In Fig. 6, the Binder cumulant of the distribution $\mathcal{P}(x)$ is plotted as function of α and d, keeping the standard deviation σ fixed. This picture qualitatively describes our data, as can be seen comparing it to Fig. 4(a). In particular, the height/width of the bump increases/shrinks as the parameter α is increased.

Lastly, we give some remarks about the connection between d and the temperature. As already observed, it must be that $d = d(\beta)$. This function should reproduce the fact that the Binder cumulant stays on the value 3 for $\beta \ll \beta_c$, it should let the bump occur for $\beta \lesssim \beta_c$ and it should make the Binder take the correct value for $\beta = \beta_c$. Since we know that B_4 is 3 for $d \to 0$, then the first aspect can be reproduced choosing a function of β that is almost zero for $\beta \ll \beta_c$. The other two properties, instead, could be obtained observing that the bump in Fig. 6 occurs before $d = 1$ and that for $d = 1$ the dependence of $B_4[\mathcal{P}(x)]$ on α drops out,

$$B_4[\mathcal{P}(x)]_{d=1} = 3 - \frac{6}{(2 + 3\sigma^2)^2}. \tag{9}$$

Then, one could choose the function $d(\beta)$ such that $d(\beta_c) = 1$ and choose σ in order to have the desired value of the Binder cumulant at the critical temperature. For the case of interest, i.e. when the Roberge-Weiss endpoint is a triple point and $B_4 = 1.5$, one should choose in our simple model $\sigma = 0$, which is clearly not allowed on finite volumes. Nevertheless, the standard deviation is known to go to zero in the thermodynamic limit, when the Binder cumulant takes the universal value. We will come back to

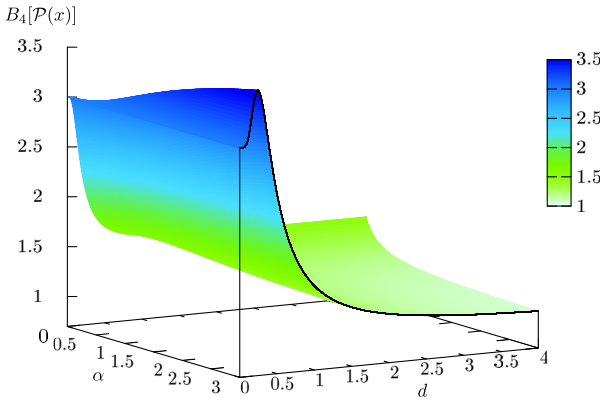

FIG. 6. Binder cumulant of the distribution in Eq. (4) for $\sigma = 0.1$ with the weights of Eqs. (7).

this aspect later in the section. For the moment, if we just decide to reproduce our data, we have to set B_4 to the measured value, that is usually higher than the theoretical one (as observed in Refs. [2,5]). For example, in Figs. 4(b), 5(b) and 6, we fixed $\sigma = 0.1$, which would mean $B_4(\beta_c) \simeq 1.544$ only slightly higher than 1.5. Instead, the value $B_4(\beta_c) = 1.68$ extracted from our data at $\kappa = 0.165$ would lead to a not so large $\sigma \simeq 0.21$, yet larger than suggested by the actual data. Another property that the function $d(\beta)$ should reproduce is the fact that for larger N_σ the transition happens faster. We already noticed that α reproduces this feature in our model. Hence, it makes sense to assume $\alpha \propto N_\sigma$ and to let d depend also on α. As a function of β, $d(\alpha, \beta)$ has to change more drastically around β_c for increasing values of α. One possibility which also fulfills the requirements for $\beta \to 0$ and for $\beta = \beta_c$ is

$$d(\alpha, \beta) = \frac{e^{\alpha\beta} - 1}{e^{\alpha\beta_c} - 1}.$$

Inserting this choice in the expression of $B_4[\mathcal{P}(x)]$, it is possible to plot the Binder cumulant as a function of β for fixed $\sigma = 0.1$ and for some values of α (that plays the role of N_σ). This has been done in Fig. 4(b). The similarity to Fig. 4(a) is evident. In particular, in both figures, the bump shrinks, and its height grows as the volume is increased. Naturally, it is also possible to take the thermodynamic limit, which means letting $\alpha \to \infty$. To do that, it is sufficient to notice that

$$\lim_{\alpha\to\infty} \alpha^m [d(\alpha, \beta)]^n = \lim_{\alpha\to\infty} \alpha^m e^{n\alpha(\beta-\beta_c)} = \begin{cases} 0, & \beta < \beta_c \\ \infty, & \beta > \beta_c \end{cases}$$

for integers $n > 0$ and $m \geq 0$. Using this relation in the expression of the Binder cumulant, we get

$$\lim_{\alpha\to\infty} B_4[\mathcal{P}(x)] = \begin{cases} 3 & \text{for } \beta < \beta_c \\ 1 & \text{for } \beta > \beta_c, \end{cases} \tag{10}$$

which is exactly the expected behavior in the thermodynamic limit. At $\beta = \beta_c$, we already showed in Eq. (9) that the Binder cumulant does not depend on α and that fixing σ to some finite, small value brings it to $B_4 > 1.5$, i.e. not exactly the universal value. Nevertheless, it is sufficient to assume $\sigma \propto \alpha^{-1}$ to completely reproduce the physical situation. In particular, this means that the standard deviation goes to zero for $\alpha \to \infty$, which implies

$$\lim_{\alpha\to\infty} B_4[\mathcal{P}(x)]_{\beta=\beta_c} = 1.5$$

[observe how the limits in Eq. (10) are still valid assuming σ proportional to α^{-1}]. The Binder cumulant bump is then nothing but a finite size effect! This suggests that also the larger than expected value $B_4(\beta_c, \infty)$ is due to these corrections.

V. NUMERICAL RESULTS AND DISCUSSION

To get a first impression about the nature of the phase transition, we produced collapse plots of the susceptibilities at each value of κ according to Eq. (3), where the norm $\|L\|$ of the Polyakov loop was used as an observable. Because of the different numerical values of the ratios γ/ν for a first- and a second-order phase transition, the collapse plots usually help to exclude one scenario. However, especially for low N_σ, the collapse plots of the susceptibilities are often inconclusive, and we complement them with collapse plots of the Binder cumulant of the imaginary part of the Polyakov loop according to Eq. (2). In Fig. 7, we show examples at $\kappa = 0.1$, $\kappa = 0.13$ and $\kappa = 0.165$ with first-order exponents in the left column and second-order exponents in the right column. In each case, the quality of the collapse clearly prefers one set of critical exponents. This indicates that $\kappa = 0.1$ and $\kappa = 0.165$ are in the first-order region, while $\kappa = 0.13$ is in the second-order region. Note how the Binder cumulant takes values larger than 3 for the first-order κ, as discussed in the previous section, while it does not for the intermediate ones.

The collapse plot technique is useful as an orientation, but it is only self-consistent, and we also wish to actually calculate the critical exponents. Thus, we fit the Binder cumulant data to Eq. (2), obtaining the critical exponent ν as a fit parameter. In order to have objective fitting criteria and avoid "fits by eye," we developed an intricate procedure which is detailed in Appendix B. Figure 8 shows the values of ν extracted from the fits, plotted as a function of κ. As expected, ν changes from first- to second-order values and back again. This behavior approaches a step function in the thermodynamic limit but remains smoothed out when the lattice volume is finite. In particular, this means that ν can in principle take any value between the universal ones in the crossing region, while far away from the tricritical masses, it is compatible with $1/3$ (first order) for small and large κ and with 0.6301(4) (second order) for intermediate κ. From the fit, the value of the Binder cumulant at the critical coupling in the infinite volume limit, $B_4(\beta_c, \infty)$, can be extracted as well. In agreement with previous studies both with staggered fermions [2] and with Wilson fermions [5], this value is slightly higher than the universal one, due to finite volume corrections as discussed in Sec. IV. However, the critical exponent ν suffers much less from this problem and is well suited to understand the nature of the phase transition. In accordance with these expectations, we estimate the two tricritical values of κ as

$$\kappa^{\text{tricr}}_{\text{heavy}} = 0.11(1), \qquad \kappa^{\text{tricr}}_{\text{light}} = 0.1625(25). \tag{11}$$

For comparison, the results from $N_\tau = 4$ [5] are also shown in Fig. 9(a). In accord with expectations, both tricritical (bare) masses move to smaller values on the finer lattice. To convert these findings into universal and

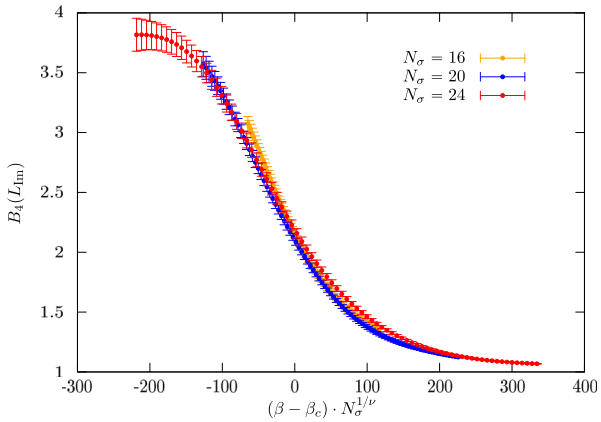

(a) $\kappa = 0.1$, first-order coefficients.

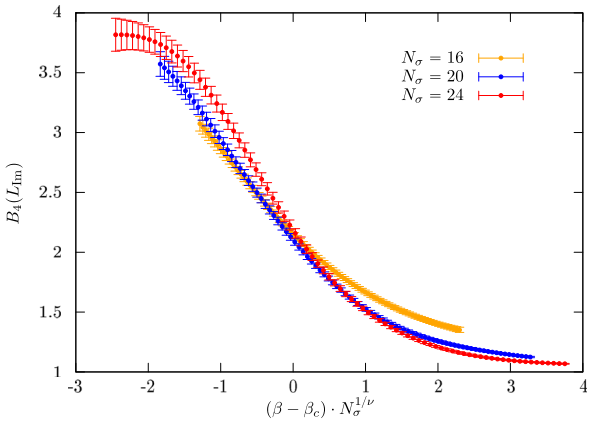

(b) $\kappa = 0.1$, second-order coefficients.

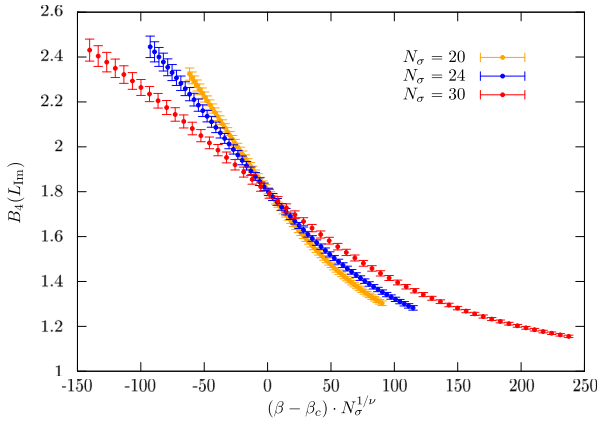

(c) $\kappa = 0.13$, first-order coefficients.

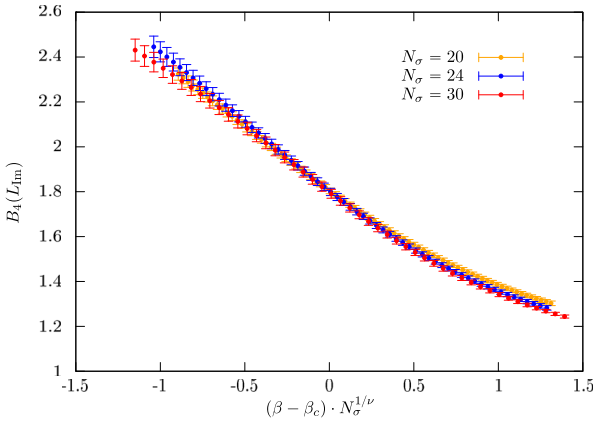

(d) $\kappa = 0.13$, second-order coefficients.

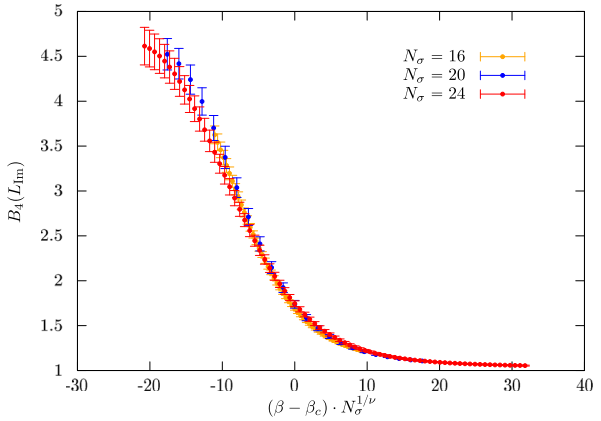

(e) $\kappa = 0.165$, first-order coefficients.

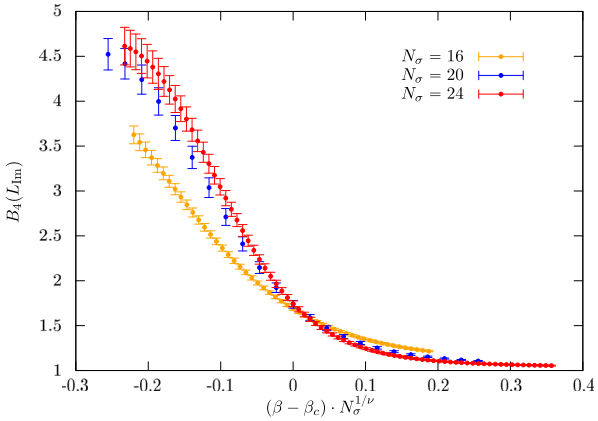

(f) $\kappa = 0.165$, second-order coefficients.

FIG. 7. Example of collapse plots of the Binder cumulant of the imaginary part of the Polyakov loop.

physical units, we set the scale at or close to the respective β_c for the relevant κ. The results for the lattice spacing a, the critical temperature T_c and m_π are summarized in Table II. Since the scale setting method using w_0 is much more precise than using the ρ mass as in Ref. [5], we evaluated again the $T = 0$ simulations from the latter study and include them here for completeness. In addition, we performed $T = 0$ simulations for the $N_\tau = 4$ $\kappa^{\rm tricr}_{\rm heavy}$ values. The lattices coarsen going to lower masses, since β decreases. All lattices considered are coarse, 0.12 fm $\lesssim a \lesssim$ 0.18 fm. However, compared to the $N_\tau = 4$ simulations, where $a \gtrsim 0.19$ fm, a clear decrease in a is achieved, as expected. Note that $m_\pi L > 6$ for all our parameter sets, so that finite size effects are negligible.

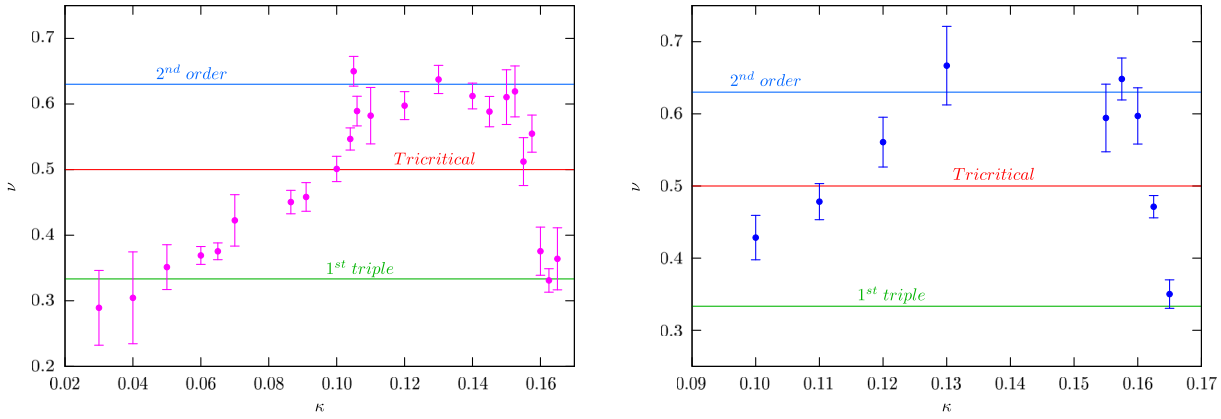

(a) $N_\tau = 4$, result of Ref. 5. (b) $N_\tau = 6$, data of present work.

FIG. 8. Critical exponent ν as function of κ. The horizontal colored lines are the critical values of ν for some universality classes. Note the different scale on the κ-axis. Due to the much higher numerical cost, not all the κ values simulated for $N_\tau = 4$ have been considered for $N_\tau = 6$. Refer to Fig. 9(a) for a more direct comparison.

Our estimates of the tricritical points in physical units for the given lattice spacing then read

$$m_\pi^{\text{tricr heavy}} = 3659^{+589}_{-619}\ \text{MeV},$$
$$m_\pi^{\text{tricr light}} = 669^{+95}_{-81}\ \text{MeV}.$$

Note that the heavy masses in lattice units are much larger than 1. Hence, the continuum mass estimates still suffer from large cutoff effects. Thus, the quoted number for $m_\pi^{\text{tricr heavy}}$ still contains a large systematic error, and a quantitative evaluation of its shift from coarser lattices is impossible. On the other hand, the shift in the lower tricritical mass is from $m_\pi \approx 910$ MeV to $m_\pi \approx 670$ MeV, or around 35%. By contrast, the critical temperature T_c does not seem to depend much on N_τ and stays roughly constant at around 200 MeV.

Our shifts in the tricritical pion masses are of similar magnitude as those in the $N_f = 3$ critical pion masses at $\mu = 0$ with Wilson Clover fermions [25]. Comparing our results to Ref. [4], one sees that our lighter tricritical mass on $N_\tau = 6$ is still higher than the staggered estimate from $N_\tau = 4$, which is roughly 400 MeV. Altogether, this shows that $N_\tau \leq 6$ is still far from the region where linear cutoff effects dominate in the standard Wilson action and suggests that drastically larger N_τ are required for both discretizations. This is expected from studies of the equation of state, where different discretizations start to agree at $N_\tau \gtrsim 12$ only (see Ref. [26] for a recent overview).

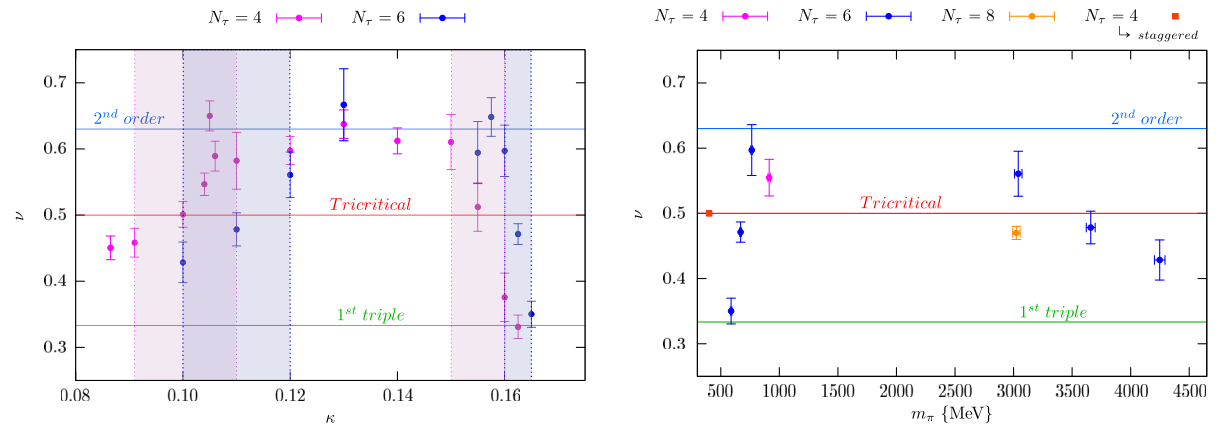

(a) $N_\tau = 4$ and $N_\tau = 6$ results. (b) Results in terms of m_π.

FIG. 9. Direct comparison between $N_\tau = 4$ and $N_\tau = 6$ results and comparison of $N_\tau = 4, 6, 8$ results in terms of m_π. In the latter case, the value of $\kappa_{\text{light}}^{\text{tricr}}$ from Ref. [4] has been included as well. For the sake of clarity, not all the $N_\tau = 4$ points have been included. The vertical colored bands highlight the position of the tricritical masses. A shift toward small masses (i.e. bigger κ) is evident as N_τ is increased.

As a first step toward larger N_τ, we also performed simulations at $N_\tau = 8$ and $\kappa = 0.13$, with $N_\sigma = 16$, 24, 32, 40, corresponding to aspect ratios of 2–5, (for details, see Appendix A). The computational costs increase dramatically with N_τ, and the statistics gathered for the $N_\sigma = 40$ simulations is not as high as for the previous simulations. However, ν can be determined in a solid fashion using the data for the other three spatial volumes, giving a value of $\nu = 0.47(1)$. The lattice spacing a is now reduced from $\approx$0.12 fm to $\approx$0.09 fm. In physical units, this new point is located at $m_\pi = 3024(32)$. Given the same caveats discussed for $N_\tau = 6$, this again suggests a large shift for the heavy tricritical mass. Note that T_c stays again constant when going from $N_\tau = 6$ to 8. Our findings are summarized in Fig. 9(b), which compares the tricritical regions for the different N_τ. Also included is the $N_\tau = 4$ value from staggered studies [4]. The figure makes apparent that much larger N_τ are required in order to go to the continuum.

VI. CONCLUSIONS

We have extended previous studies of the nature of the Roberge-Weiss end point of $N_f = 2$ QCD at imaginary chemical potential to $N_\tau = 6$ and for one mass value to $N_\tau = 8$, using standard Wilson fermions. To this end, we gathered large amounts of data for several volumes and carried out a thorough finite size analysis. In particular, we have understood the occurrence of a "bump" in the Binder cumulant in the region where the Roberge-Weiss end point is a triple point. The behavior can be explained as a finite size effect specifically due to the merging of a three-peak distribution to a two peak distribution as a function of the lattice coupling.

The qualitative phase structure fully replicates that on the coarser $N_\tau = 4$ lattices. However, the tricritical pion mass values separating the regime of a second-order end point from triple points in the small and large mass regions shift considerably when the cutoff is reduced and suggest that significantly finer lattices are necessary before the observed phase structure settles quantitatively in the continuum.

ACKNOWLEDGMENTS

We thank the staff of LOEWE-CSC and L-CSC for its support, Andrei Alexandru for early discussions and Frederik Depta for the code to extract the pion mass. C. C, O. P., C. P. and A. S. are supported by the Helmholtz International Center for FAIR within the LOEWE program of the State of Hesse. C. C. is supported by the GSI Helmholtzzentrum für Schwerionenforschung. F. C. and O. P. are supported by the German BMBF under Contract No. 05P1RFCA1/05P2015 (BMBF-FSP 202).

APPENDIX A: SIMULATION DETAILS

A detailed overview of all our simulation runs is provided in Table III. Measurements of the Binder cumulant are difficult because of the large autocorrelations involved and the large statistics required. For a generic observable x, the sets of measurements $\{x_i\}, \{x_i^2\}, \ldots, \{x_i^n\}$ show different integrated autocorrelation times τ_{int}, which we estimated using the Wolff algorithm [27]. Dividing the total number of Hybrid Monte Carlo trajectories by τ_{int} gives the number of independent measurements for a given observable. We collected at least 30 independent events per run of a given parameter set for $B_4(L_{\mathrm{Im}})$. In addition, we ran the same parameter set generating typically four independent Markov chains until $B_4(L_{\mathrm{Im}})$ was compatible within three standard deviations between all of them. Figure 10 shows an example at $\kappa = 0.1625$ on $N_\sigma = 18$. The improvement of the signal with statistics is clearly visible.

TABLE III. Overview of the statistics accumulated in all the simulations ($N_\tau = 6$ and $\mu_i = \pi/6$). Since the resolution in β is not the same at different κ, the number of simulated β has been reported per each range. The accumulated statistics per β has not always been the same. Therefore, the number of trajectories here is about all the trajectories produced per given N_σ. Using the number of chains provided above, it can be easily estimated how long each chain was on average, even though we always accumulated higher statistics close to the critical temperature.

			Total statistics per spatial lattice size N_σ (# of simulated β values | # of chains)				
N_τ	κ	β range	16 **18**	20	24	30 **32**	12 **36** *40*
	0.1000	5.8460–5.9020	6.11M (24 | 2)	4.36M (16 | 2)	4.30M (16 | 2)	⋯	⋯
	0.1100	5.8400–5.8660	⋯	3.81M (26 | 4)	1.49M (14 | 4)	4.05M (18 | 4)	**1.92M** (**13** | **4**)
	0.1200	5.8180–5.8450	5.28M (10 | 4)	3.89M (9 | 4)	3.23M (9 | 4)	2.19M (8 | 4)	⋯
	0.1300	5.7760–5.7980	⋯	3.94M (25 | 4)	3.76M (23 | 4)	3.56M (16 | 4)	⋯
6	0.1550	5.5210–5.5420	1.40M (30 | 1)	1.04M (23 | 1)	1.12M (24 | 1)	0.76M (9 | 4)	⋯
	0.1575	5.4750–5.4930	**0.59M** (**7** | **4**)	⋯	0.92M (7 | 4)	1.40M (7 | 4)	⋯
	0.1600	5.4330–5.4430	**0.52M** (**6** | **4**)	⋯	0.86M (6 | 4)	1.12M (6 | 4)	⋯
	0.1625	5.3800–5.3930	**0.92M** (**12** | **4**)	⋯	1.12M (8 | 4)	⋯	1.38M (7 | 4)
	0.1650	5.3260–5.3370	1.99M (16 | 4)	1.09M (11 | 4)	1.71M (12 | 4)	⋯	⋯
8	0.1300	5.9400–5.9800	**3.69M** (**9** | **4**)	⋯	5.40M (9 | 4)	**2.00M** (**5** | **4**)	*1.00M* (*5* | *4*)

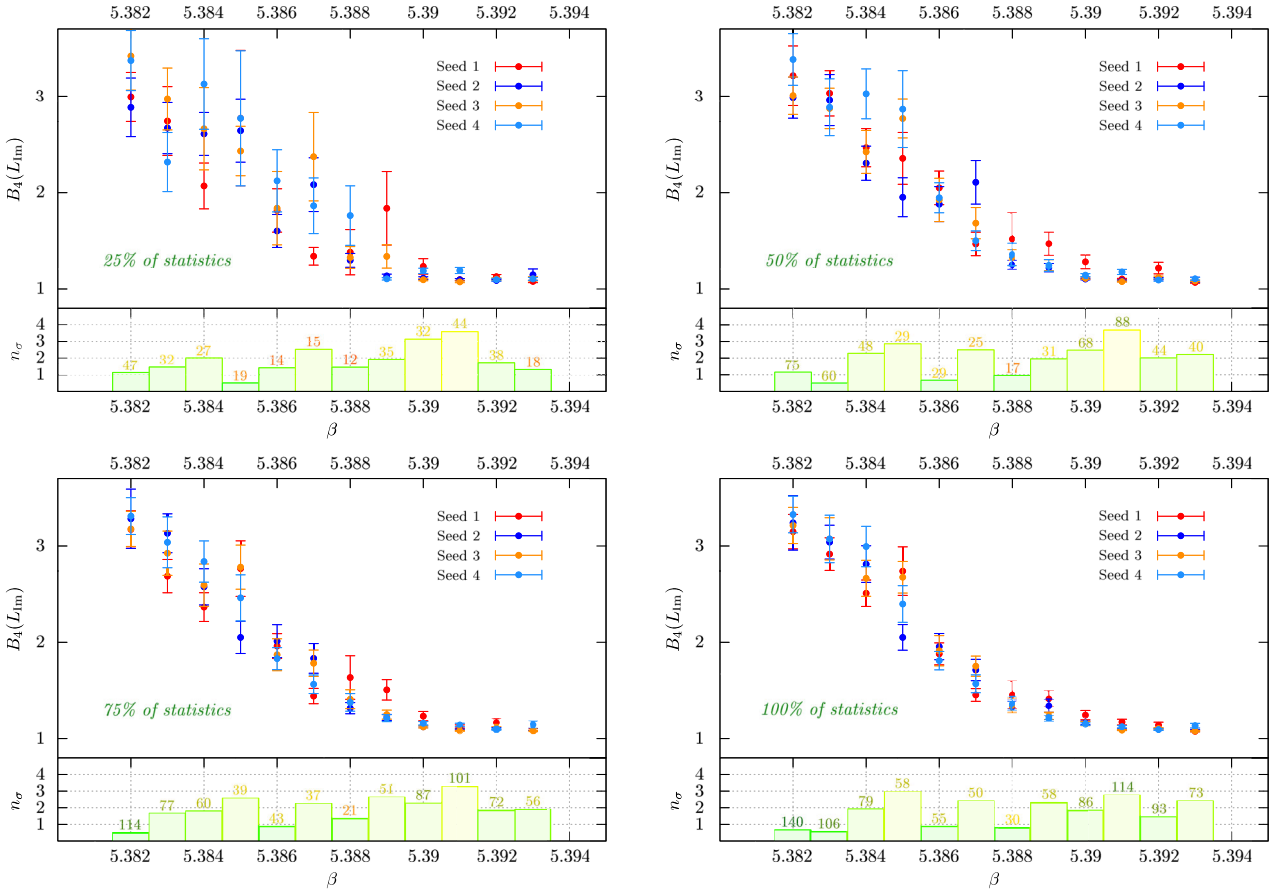

FIG. 10. Successive analysis of the Binder cumulant measurements at $\kappa = 0.1625$ on $N_\sigma = 18$. The histogram below each plot is a guideline to judge on the statistics. n_σ at each β is the number of standard deviations at which the two most different chains are compatible. The number above each bar is the average number of independent events collected at that β. The colors have been chosen in order to reflect the goodness of the statistics: from green (statistics high enough) to red (statistics to be increased). Both n_σ and the number of independent events have to be monitored to decide when to stop increasing statistics.

Once each chain was long enough, we merged them for the finite size scaling analysis.

APPENDIX B: EXTRACTING THE CRITICAL EXPONENT ν

As described in Sec. III, we extracted the critical exponent ν fitting the $B_4(L_{\rm Im})$ data for different spatial lattice sizes according to Eq. (2). Because of the numerical cost, the number of simulated β's is limited. If the distributions of $\mathcal{S}_g(\beta_1)/\beta_1$ and $\mathcal{S}_g(\beta_2)/\beta_2$ have a good overlap, one can use Ferrenberg-Swendsen reweighting [17] to obtain our observable at $\beta_1 < \beta_{\rm new} < \beta_2$. However, increasing the number of reweighted points can arbitrarily reduce the value of the $\chi^2_{\rm NDF}$ of the fits. For this reason, we almost always reweighted our data using all simulated β's, but without adding new points, i.e. where $\beta_{\rm new}$ is one of the simulated β. Exceptions to this are the first-order regions where the Binder cumulant was very steep and a higher resolution in β was needed.

Varying the fit interval by range and location, there is a multitude of possible fits with differing results from which the "good" ones have to be chosen. Here, we outline the criteria of the filter algorithm used to select our results:

(i) We never extrapolated, i.e. all fitting intervals were placed such that

$$\beta_c \in I = [\beta_{\rm min}, \beta_{\rm max}]. \tag{B1}$$

(ii) Since the scaling variable was $x \equiv (\beta - \beta_c)N_\sigma^{1/\nu}$, the scaling region in β shrank with growing N_σ. Thus, for the fitting intervals $I_1, \ldots, I_n$ of the data with $N_{\sigma_1} < \ldots < N_{\sigma_n}$, we demanded

$$I_1 \supseteq \cdots \supseteq I_n. \tag{B2}$$

(iii) On the reduced chi-square, we imposed

$$1 - \delta \leq \chi^2 \leq 1 + \delta, \quad \text{with} \quad \delta \approx 0.2.$$

TABLE IV. Overview of the selected fits to extract the final value of ν (the bold font line refers to $N_\tau = 8$). The fits were performed according to Eq. (2), considering the linear term only. The N_σ column contains the spatial lattice extents that have been included in the fits. $\Omega_{\min}$ and $\Xi_{\min}$ are, respectively, the minimum overlap percentage and the minimum symmetry percentage of Eqs. (B3) and (B4).

κ	N_σ	β_c	ν	$B_4(\beta_c, \infty)$	a_1	χ^2_{NDF}	Q(%)	$\Omega_{\min}$	$\Xi_{\min}$
0.1000	16 20 24	5.86980(29)	0.43(3)	2.141(26)	−0.09(4)	1.034	41.51	86.70	6.67
0.1100	20 24 30 36	5.85670(10)	0.478(25)	1.766(11)	−0.14(5)	0.999	46.26	83.06	20.00
0.1200	16 20 24 30	5.82870(10)	0.56(3)	1.872(8)	−0.31(10)	1.005	45.61	87.18	86.00
0.1300	20 24 30	5.78670(20)	0.67(5)	1.818(18)	−0.72(28)	0.980	45.82	84.12	82.50
0.1300	**16 24 32**	**5.95872(26)**	**0.47(1)**	**2.048(8)**	**−0.05(1)**	**0.984**	**49.50**	**80.02**	**72.67**
0.1550	16 20 24 30	5.52840(10)	0.59(5)	1.804(14)	−0.8(3)	1.048	40.03	81.44	40.00
0.1575	18 24 30	5.48330(10)	0.648(29)	1.990(20)	−1.4(3)	0.995	47.08	88.49	92.50
0.1600	18 24 30	5.43670(10)	0.60(4)	1.781(20)	−1.5(5)	1.017	43.04	87.14	52.00
0.1625	12 18 24	5.38620(9)	0.471(15)	1.906(5)	−0.72(13)	1.004	45.52	81.61	100.00
0.1650	16 20 24	5.33477(3)	0.350(20)	1.680(7)	−0.15(7)	1.007	45.40	91.40	65.00

(iv) The fitting range in x should ideally be the same for all volumes included. We mapped the intervals I_n to intervals

$$\tilde{I}_n \equiv [x_n^{\min}, x_n^{\max}].$$

For two intervals $A = [a_1, a_2]$ and $B = [b_1, b_2]$, we defined an *overlap percentage* as

$$\Omega \equiv \begin{cases} 0 & \text{if } a_2 < b_1 \vee b_2 < a_1 \\ 100 \cdot \left(1 - \frac{|b_1 - a_1| + |b_2 - a_2|}{a_2 - a_1 + b_2 - b_1}\right) & \text{otherwise} \end{cases}. \tag{B3}$$

We then required $\Omega \geq 80\%$.

(v) Since the scaling region was based on Taylor expansion, it should be symmetric around x_c,

$$I_{\text{scaling}} = [-\bar{x}, \bar{x}],$$

with $\bar{x}$ and the size of the region only known after the fit. Given an interval $J = [-a, b]$ with a and b non-negative and $a + b$ fixed, we defined a *symmetry percentage* as

$$\Xi \equiv 100 \cdot \left(1 - \left|\frac{2a}{a+b} - 1\right|\right) = 100 \cdot \left(1 - \left|\frac{2b}{a+b} - 1\right|\right). \tag{B4}$$

Clearly, $\Xi = 0\%$ (maximally asymmetric interval) for $a = 0$ or $b = 0$, and $\Xi = 100\%$ (maximally symmetric interval) for $a = b$. Among possible fits, we chose the one with maximal Ξ.

The final list of selected fits is given in Table IV.

[1] H. Meyer, *Proc. Sci.*, LAT2015 (2015) 354.
[2] P. de Forcrand and O. Philipsen, Phys. Rev. Lett. **105**, 152001 (2010).
[3] M. D'Elia and F. Sanfilippo, Phys. Rev. D **80**, 111501 (2009).
[4] C. Bonati, G. Cossu, M. D'Elia, and F. Sanfilippo, Phys. Rev. D **83**, 054505 (2011).
[5] O. Philipsen and C. Pinke, Phys. Rev. D **89**, 094504 (2014).
[6] A. Alexandru and A. Li, *Proc. Sci.*, LAT2013 (2013) 208.
[7] A. Roberge and N. Weiss, Nucl. Phys. **B275**, 734 (1986).
[8] C. Bonati, M. D'Elia, P. de Forcrand, O. Philipsen, and F. Sanfillippo, *Proc. Sci.*, LATTICE2013 (2014) 219.
[9] O. Philipsen and C. Pinke, *Proc. Sci.*, LAT2015 (2015) 149.
[10] P. de Forcrand, S. Kim, and O. Philipsen, *Proc. Sci.*, LAT2007 (2007) 178.
[11] M. Fromm, J. Langelage, S. Lottini, and O. Philipsen, J. High Energy Phys. 01 (2012) 042.
[12] K. Binder, Z. Phys. B **43**, 119 (1981).
[13] A. Pelissetto and E. Vicari, Phys. Rep. **368**, 549 (2002).
[14] S. Duane, A. D. Kennedy, B. J. Pendleton, and D. Roweth, Phys. Lett. B **195**, 216 (1987).
[15] M. Hasenbusch, Phys. Lett. B **519**, 177 (2001).
[16] B. Joo, B. Pendleton, A. D. Kennedy, A. C. Irving, J. C. Sexton, S. M. Pickles, and S. P. Booth, Phys. Rev. D **62**, 114501 (2000).
[17] A. M. Ferrenberg and R. H. Swendsen, Phys. Rev. Lett. **63**, 1195 (1989).
[18] S. Borsanyi *et al.*, J. High Energy Phys. 09 (2012) 010.
[19] M. Bach *et al.*, https://github.com/CL2QCD/cl2qcd.
[20] Khronos Working Group, http://www.khronos.org/registry/cl/.

[21] M. Bach, V. Lindenstruth, O. Philipsen, and C. Pinke, Comput. Phys. Commun. **184**, 2042 (2013).
[22] O. Philipsen, C. Pinke, A. Sciarra, and M. Bach, *Proc. Sci.*, 038 (2014).
[23] M. Bach, M. Kretz, V. Lindenstruth, and D. Rohr, Comp. Sci. Res. Develop. **26**, 12 (2011).
[24] D. Rohr, M. Bach, G. Neskovic, V. Lindenstruth, C. Pinke, and O. Philipsen, *High Performance Computing (LNCS): 30th International Conference, ISC High Performance 2015, Frankfurt, Germany* Vol. 9137 (Springer International Publishing, Cham, 2015), pp. 179–196.
[25] X.-Y. Jin, Y. Kuramashi, Y. Nakamura, S. Takeda, and A. Ukawa, Phys. Rev. D **91**, 014508 (2015).
[26] O. Philipsen, Prog. Part. Nucl. Phys. **70**, 55 (2013).
[27] U. Wolff (ALPHA Collaboration), Comput. Phys. Commun. **156**, 143 (2004); **176**, 383(E) (2007).